Accepted Manuscript

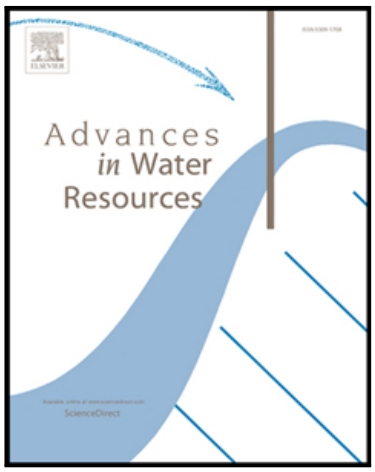

Water sorptivity of unsaturated fractured sandstone: fractal modeling and neutron radiography experiment

Yixin Zhao , Yang Wu , Songbai Han , Shanbin Xue , Guowei Fan , Zhongwei Chen , A. El Abd

PII: S0309-1708(19)30182-4
DOI: https://doi.org/10.1016/j.advwatres.2019.06.006
Reference: ADWR 3361

To appear in: *Advances in Water Resources*

Received date: 28 February 2019
Revised date: 9 June 2019
Accepted date: 9 June 2019

Please cite this article as: Yixin Zhao , Yang Wu , Songbai Han , Shanbin Xue , Guowei Fan , Zhongwei Chen , A. El Abd , Water sorptivity of unsaturated fractured sandstone: fractal modeling and neutron radiography experiment, *Advances in Water Resources* (2019), doi: https://doi.org/10.1016/j.advwatres.2019.06.006

Highlights

- Water imbibition within fractured sandstone was visualized by neutron radiography.
- The loss coefficient was introduced to explain water losses from fracture to matrix.
- A new fractal model was established to predict the rough-walled fracture sorptivity.
- A new method was provided to estimate the time exponent of rough-walled fracture.

Water sorptivity of unsaturated fractured sandstone: fractal modelling and neutron radiography experiment

Yixin Zhao[a,b,c]*, Yang Wu[a,c]*, Songbai Han[d], Shanbin Xue[a,b], Guowei Fan[a,b], Zhongwei Chen[e], A. El Abd[f]

*Corresponding Authors: (Zhao Y) zhaoyx@cumtb.edu.cn; (Wu Y) wuyangln@163.com

[a] Beijing Key Laboratory for Precise Mining of Intergrown Energy and Resources, China University of Mining and Technology (Beijing), Beijing 100083, China

[b] State Key Laboratory of Coal Resources and Safe Mining, China University of Mining and Technology, Beijing 100083, PR China

[c] School of Energy & Mining Engineering, China University of Mining and Technology, Beijing 100083, PR China

[d] Neutron Scattering Laboratory, China Institute of Atomic Energy, Beijing 102413, PR China

[e] School of Mechanical and Mining Engineering, The University of Queensland, St Lucia, QLD 4072, Australia

[f] Reactor Physics Department, Nuclear Research Centre, Atomic Energy Authority, 13759, Cairo, Egypt

Abstract

The spontaneous imbibition of water into the matrix and gas-filled fractures of unsaturated porous media is an important phenomenon in many geotechnical applications. Previous studies have focused on the imbibition behavior of water in the matrix, but few works have considered spontaneous imbibition along fractures. In this work, a new fractal model, considering the water losses from the fracture to the matrix, was established to predict the sorptivity of rough-walled fracture. A fractal model, considering the fractal dimension of tortuosity, was modified to estimate the sorptivity of the matrix. Both of the models have a time exponent α and can be simplified to the classical Lucas–Washburn (L–W) equation with α = 0.50. To verify the proposed models, quantitative data on the imbibition of water in both the matrix and the fracture of unsaturated sandstone were acquired by neutron radiography. The results show that the motion of the wetting front in both the matrix and the fracture does not obey the L–W equation. Both theory and experimental observations indicate that fracture can significantly increase spontaneous imbibition in unsaturated sandstone by

capillary action. Compared with the classical L–W equation, the models proposed in this study offers a better description of the dynamic imbibition behaviour of water in unsaturated fractured sandstone and, thus, more reliable predictions of the sorptivity of the matrix and the fracture. Moreover, a new method to estimate the time exponent of rough-walled fracture in sandstone was also provided.

Keywords: sorptivity, neutron radiography, rough-walled surface, time exponent, fractal model

1. Introduction

Understanding the migration of liquid in the matrix and fractures of an unsaturated porous medium has great significance to many geotechnical applications (Aydin, 2000), such as radioactive waste storage (Bodvarsson et al., 1999; Hunt and Tompson, 2005; Tompson et al., 2006), sequestration of carbon dioxide (Doster et al., 2013; Herring et al., 2013), unconventional gas extraction, oil and geothermal recoveries (Karpyn et al., 2009b; Li and Horne, 2001; Serhat and Kovscek, 1999), the protection of building foundations and other structures in the water environment (Cnudde et al., 2008; Daniel et al., 2015), and the protection of groundwater resources (Faybishenko et al., 2005). In recent years, the application of rapid real-time neutron radiography and high-resolution X-ray computed tomography (CT) imaging technology has greatly enhanced our experimental capability in studying liquid flow in porous media. Rapid real-time neutron radiography shows unique advantages (Kang et al., 2013) over other techniques owing to the strong attenuation of neutron rays by hydrogen and its relative insensitivity to the gas phase (only valid for non-Hydrogen gases) and mineral composition (e.g., quartz and clay). The microporous structure of porous media can be described accurately by high-resolution X-ray CT imaging technology (Zhao et al., 2017). As a result, researchers can characterise the flow of liquids in the matrix and fracture zone of porous media at high spatial and temporal resolutions and quantify the distribution of water in a wide range of natural and engineering materials.

Neutron radiography has been used in many studies to analyse water migration and distribution in porous media, such as rock (Dewanckele et al., 2013; Kang et al., 2013a; Cheng et al., 2015; Zhao et al., 2017), brick (Czachor et al., 2002; El Abd et al., 2009; Hassanein et al., 2006; Karoglou et al., 2005), and concrete (Zhang et al., 2011, 2010a, 2010b, 2009). However, most of the previous studies focused on the spontaneous imbibition of porous media matrices, whereas few studies exist on the spontaneous imbibition of fracture structures. Water imbibition into fracture structures—such as the compacted shear band of sandstone cores (Hall, 2013), air-filled fractures in sandstone (Cheng et al., 2015), or steel-reinforced concrete

(Zhang et al., 2010a)—is rapid, in contrast to that occurring in matrices. The results of the above studies show that the relationship between the imbibition height of the wetting front in the matrix or fracture of the porous media and time obeys the Lucas–Washburn (L–W) equation (i.e., the height of the wetting front is proportional to the square root of the time). Accordingly, the sorptivity of matrix and fractures can be obtained by linear regression or by direct calculation from the L–W equation. However, the dynamic evolution of the wetting front does not always follow the L–W equation. For example, the wetting behaviour of lubricating oil in wool blankets and cotton fabrics usually does not obey the L–W law. The change of pore structure in porous media (Balankin and Susarrey, 2003) or the disorder of the capillary pressure caused by the anisotropy of the medium and the randomness of the pore size (Brú and Pastor, 2006) may be the main causes of this phenomenon. Thus, a modified L–W equation, which assumes that the imbibition height of the wetting front is proportional to the power α of the time (α is the time exponent), has been proposed (Laughlin and Davies, 1961). The validity of the modified L–W equation was later confirmed by a number of experimental results (Balankin and Susarrey, 2003; Brú and Pastor, 2006).

Based on fractal theory, an analytical expression of water imbibition in tortuous capillary tubes was derived, in which the time exponent can be expressed as a function of the fractal dimension of tortuosity of the flow line in porous media (Cai and Yu, 2011). This analytical expression can be used to describe the dynamic imbibition of water in the porous media matrix and calculate the matrix sorptivity. Nevertheless, for the imbibition behaviour of water within fractures of porous media, some of the above observations are qualitatively explained from the dynamics of capillary uptake (Cheng et al., 2015; Hall, 2013; Zhang et al., 2010a). However, to our knowledge, there seems to be no theoretical framework in the literature for the quantitative interpretation of water imbibition in fractures of porous media. The study of this phenomenon is likely to be particularly important for engineering applications, such as for the calculation of water losses in the exploitation of unconventional gas resources (e.g., sandstone/shale gas) by using hydraulic fracturing and water damage to the foundations of buildings and other structures (Cheng et al., 2015). The major

objectives of this research are: (i) to modify a model to predict the sorptivity of matrix, which takes into account the fractal dimension of tortuosity; (ii) to establish a fractal model to predict the sorptivity of a rough-walled fracture in the unsaturated sandstone, which considers the water losses from the fracture to the matrix; (iii) to acquire quantitative data of the spontaneous imbibition of water in unsaturated fractured sandstone specimen using dynamic neutron radiography and use them to evaluate the proposed models.

2. Theoretical Framework

The phenomenon of water imbibition in porous media has been studied since the beginning of the 20th century. The L–W equation was derived to describe the water imbibition in a single capillary tube by using the Hagen–Poiseuille equation, which lays the foundation for the study of water imbibition in the pore structure of a porous media matrix (Lucas, 1918; Washburn, 1921). Cai et al. (2010) modified the L–W equation and then represent a porous medium as a bundle of tortuous capillary tubes to predict the dynamic imbibition of water in the matrix of the porous medium. However, in addition to the pore structure, many other fracture structures exist in porous media, such as rocks. Several classical theories have been established to describe the spontaneous imbibition of porous media, but most of them just focus on the imbibition of pore structures (Benavente et al., 2002; Cai et al., 2014; Hammecker et al., 2004; Joekar-Niasar et al., 2010; Leventis et al., 2000; Li and Zhao, 2012) and few have concentrated on fracture structures (Cheng et al., 2015). Hardly any general models have been established to calculate the sorptivity of the fractures of a porous medium. For this purpose, a fractal model based on tortuous capillary bundle was further developed to describe the imbibition of water in sandstone matrix, and a fractal model, considering the water loss from the fracture into the matrix, was established to describe the imbibition of water in fracture of sandstone.

2.1 A fractal model to analyse water imbibition in the matrix

In the process of imbibition, water enters the pore structures of natural porous

media under the capillary force (Cai and Yu, 2011; Cheng et al., 2015; Cnudde et al., 2008). The pore structure of natural porous media is complex, and the pore size distribution (PSD) has the essential features of a fractal system (Katz and Thompson, 1985; Krohn, 1988). This complex pore structure can be simplified as a bundle of tortuous capillary tubes with fractal characteristics (Bear, 1972; Cai et al., 2010a; Yu, 2008, 2005; Yu et al., 2008). The capillary tubes in the bundle have different diameters, and the distribution of capillary diameters within the maximum and minimum capillary diameters satisfies the fractal power ratio relationship (Yu, 2008). According to the Hagen–Poiseuille equation and the assumption of infinite mobility of air phase in the matrix, the flow rate of a single tortuous circular capillary can be expressed as:

$$Q = \frac{\pi\lambda^4 \Delta P}{128\mu L_f} \tag{1}$$

where Q is the flow rate, λ [μm] is the capillary diameter of the matrix, L_f [mm] is the fractal distance travelled by the wetting front in the capillary (as shown in Fig. 1), μ [Ns/m^2] is the viscosity of water, and ΔP represents the pressure drop along the capillary. Water is imbibed into the capillary spontaneously under the action of the pressure drop.

The effect of gravity on the early stages of spontaneous capillary imbibition can be ignored since the assumptions of negligible effects are never validated (Cheng et al., 2015; Hay and Dragila, 2008). Thus, ΔP can be expressed as:

$$\Delta P = P_c \tag{2}$$

where P_c is the capillary pressure. According to the Young–Laplace equation, P_c can be expressed as:

$$P_c = \frac{4\sigma\cos\theta}{\lambda} \tag{3}$$

where σ [N/m] is the air–water surface tension, θ [°] is the water–solid contact angle. The fractal velocity v_f [mm/s] can be obtained as follows:

$$v_f = \frac{4Q}{\pi\lambda^2} = \frac{\lambda^2 P_c}{32\mu L_f} \tag{4}$$

Combining Eq. (3) to (4) yields:

$$v_f = \frac{\lambda\sigma\cos\theta}{8\mu L_f} \tag{5}$$

In most previous applications, the relation between L_f and L_s (the straight-line vertical distance travelled by the wetting front in the capillary along the pressure drop, as shown in Fig. 1) is expressed by a constant tortuosity. However, the tortuous capillaries always exhibit the fractal behaviour in porous media. Wheatcraft and Taylor (1988) developed a proportional relationship between L_f and the length scale ε to describe the relationship between L_f and L_s. Yu and Cheng (2002) believed that the diameter of the capillaries λ is analogous to the length scale ε. Cai and Yu (2011) reported that the tortuosity depends on the scale of measurement and the fractal dimension for tortuosity of capillaries D_T. They also developed the fractal scaling relationship between L_s and λ in porous media:

$$L_f = \lambda^{1-D_T} L_s^{D_T} \tag{6}$$

where D_T lies in $1 < D_T < 2$ and $1 < D_T < 3$ in two- and three-dimensional spaces, respectively. By differentiating Eq. (6) with respect to time, the relationship between the fractal velocity $v_f = dL_f/dt$ and the straight-line velocity $v_s = dL_s/dt$ (as shown in Fig. 1) can be obtained (Cai et al., 2010a):

$$v_f = D_T L_s^{D_T-1} \lambda^{1-D_T} v_s \tag{7}$$

By substituting Eqs. (6) and (7) into Eq. (5), the water rising process in a single tortuous capillary can be expressed as follows (Cai et al., 2014, 2010a):

$$\frac{dL_s}{dt} = \frac{\lambda^{2D_T-1}\sigma\cos\theta}{8\mu D_T L_s^{2D_T-1}} \tag{8}$$

Integrating Eq. (8) assuming the initial condition $L_s(0) = 0$ yields:

$$L_s = \left(\frac{\sigma\cos\theta}{4\mu\lambda^{1-2D_T}}\right)^{\frac{1}{2D_T}} \cdot t^{\frac{1}{2D_T}} \tag{9}$$

When $D_T = 1$ (straight capillary, as shown in Fig. 1), we obtain the L–W equation, which is expressed as:

$$L_s = \left(\frac{\lambda \sigma \cos\theta}{4\mu} \right)^{\frac{1}{2}} \cdot t^{\frac{1}{2}} \tag{10}$$

Cai and Yu (2011) obtained the relationship between time exponent α and the D_T (i.e., $\alpha=1/(2D_T)$. Thus, the D_T can be expressed as a function of time exponent α as follows:

$$D_T = \frac{1}{2\alpha} \tag{11}$$

Then, Eq. (9) can be simplified as:

$$L_s = \left(\frac{\sigma \cos\theta}{4\mu\lambda^{1-1/\alpha}} \right)^{\alpha} \cdot t^{\alpha} \tag{12}$$

For a bundle of tortuous capillary tubes with different diameters, the average distance travelled by the wetting front L_{sm} [mm] can be calculated by the following expression (Cai and Yu, 2011):

$$L_{sm} = t^{\alpha} \int_{\lambda_{min}}^{\lambda_{max}} f(\lambda) \left(\frac{\sigma cos\theta}{4\mu\lambda^{1-1/\alpha}} \right)^{\alpha} d\lambda = C_m t^{\alpha} \tag{13}$$

where $f(\lambda)$ is the probability density function of the capillary diameter, defined as $f(\lambda) = D\lambda_{min}^{D}\lambda^{-(D+1)}$. D is the pore fractal dimension (Yu, 2008). λ_{max} [μm] and λ_{min} [μm] are the maximum and minimum pore diameters, respectively. The value of λ_{max} [μm] can be calculated by using the expression as follows (Cai et al., 2010a):

$$\lambda_{\max} = \sqrt{32\tau K \frac{4-D}{2-D} \frac{1-\phi}{\phi}} \tag{14}$$

where τ is the tortuosity of pore structure, K [mD] is the permeability, Φ is the porosity. C_m is the sorptivity of the matrix, which can be expressed as:

$$C_m = \left(\frac{\sigma cos\theta}{4\mu} \right)^{\alpha} \cdot \frac{D\lambda_{max}^{(1-\alpha)}}{1-D-\alpha} \left(\beta^{D} - \beta^{(1-\alpha)} \right) \tag{15}$$

where β is defined as $\lambda_{min}/\lambda_{max}$ and generally it has a value of $10^{-4} \le \beta \le 10^{-2}$ in porous media (Cai et al., 2010b; Feng et al., 2004; Yu and Li, 2001). Based on this theoretical framework, Eq. (15) is used to predict the sorptivity of the matrix in fractured sandstone. In the applications, time exponent α can be obtained by experimental data fitting.

2.2 A fractal model to analyse water imbibition in a fracture zone

In general, water imbibition is rapidly in a rough fracture. Cheng et al. (2015) believed that this phenomenon is caused by the combination of the capillary force and the surface spreading effect. Hay and Dragila (2008) idealized the rough surface as comprised of a series of small cylindrical posts lined up on an otherwise smooth surface and then derived an invasion model to describe the spreading of water in a rough surface. Their assumption considered the effect of rough surface on water spreading. However, in natural rocks, the fractures are not only rough but also tortuous. In this section, we assume that the fracture is a tortuous capillary with a rough surface and filled with air. The top of the fracture is dry until the fracture filled with water, thus, the driving force is always the maximum capillary force during the imbibition process (Andersen et al., 2018b). Since the fracture is filled with air, the mobility ratio is strongly favourable (Andersen et al., 2018b) and the piston-like displacement occurs during the imbibition of water into the fracture. The rough surface is idealized as comprising a series of small cylinders arranged on a curved smooth surface, and we assume that the height of the cylinder δ [μm] is equal to the average sand grain diameter of specimen W1. The distance between the cylinder edges ξ [μm] and the diameter of the cylinder d [μm] is 2.08δ and 0.83δ, respectively (Hay et al., 2008). The cross-sectional flow model is shown in Fig. 2(b). According to this assumption, a fractal model is established to describe the rapid uptake of water within a single vertical fracture. To obtain the flow rate of a single fracture, Eq. (1) can be modified and expressed as:

$$Q = \frac{(1-\gamma)\pi\lambda_f{}^4\Delta P}{128\mu L_{ff}} \tag{16}$$

where λ_f [μm] is the median aperture of fracture, L_{ff} [mm] is the fractal distance travelled by the wetting front in fracture. γ is the water loss coefficient, which means the percentage of water imbibed from the fracture into the matrix and can be expressed as:

$$\gamma = \frac{V_{m1}+V_{m2}}{V_f+V_{m1}+V_{m2}} = \frac{A_s(H_{sm1}+H_{sm2})\phi\bar{\theta}_w}{A_f L_{sf}+A_s(H_{sm1}+H_{sm2})\phi\bar{\theta}_w} = \frac{(H_{sm1}+H_{sm2})\phi\bar{\theta}_w}{\lambda_f+(H_{sm1}+H_{sm2})\phi\bar{\theta}_w} \tag{17}$$

where V_f [mm^3] is the volume of water that imbibed into the fracture. V_{m1} and V_{m2} [mm^3] are the volumes of water imbibed into the matrix from the left and right walls of the fracture, respectively. H_{sm1} and H_{sm2} [mm] are the horizontal distances travelled by the wetting front in the matrix on the left and right walls of the fracture, respectively. $\bar{\theta}_w$ [mm^3/mm^3] is the average volumetric water content. A_s [mm^2] and A_f [mm^2] is the fracture-matrix vertical cross-sectional area and the horizontal cross-sectional area of the fracture, respectively. L_{sf} [mm] is the straight-line distance travelled by the wetting front in the fracture. The above parameters related to caculate γ can be obtained by experiment, such as neutron radiography test. Due to the rough surface of the fracture, the pressure drop ΔP can be expressed as:

$$\Delta P = P_c + 2\Delta P_c - 2P_\mu \tag{18}$$

where $\triangle P_c$ is the pressure difference across the water–air interface caused by capillarity in rough surface, which drives the spread of water in rough surface. According to Young-Laplace equation, $\triangle P_c$ can be expressed as (Hay et al., 2008):

$$\Delta P_c = \sigma\left(\frac{1}{R_\delta} + \frac{1}{R_\xi}\right) \tag{19}$$

where R_δ and R_ξ are the radii of curvature in the vertical and the horizontal directions (see Fig. 2(a)). Here, we assume that the roughness elements (i.e., cylinders) are normal to the surface. Thus, the radii of curvature R_δ and R_ξ are defined as:

$$\begin{aligned} R_\delta &= \frac{\delta}{\cos\theta - \sin\theta} \\ R_\xi &= \frac{\xi}{2\cos\theta} \end{aligned} \tag{20}$$

P_μ is the loss of pressure due to viscous dissipation, which can be given as (Hay et al., 2008):

$$P_\mu = \frac{2P_0\mu L_{sf} v_f}{d_h^2} \tag{21}$$

where L_{sf} [mm] is the straight-line distance of water imbibition in the fracture, which can be expressed as $L_{sf} = L_{ff}/\tau_f$, and τ_f is the tortuosity of the fracture. The Poiseuille number, $P_0 = C_F Re$, where C_F is the Fanning friction factor and Re is the Reynolds

number associated with the diameter length scale (P_0 = 14.38 for a rectangle with an aspect ratio of δ/λ = 0.48). d_h [μm] is the hydraulic diameter, defined as:

$$d_h = \frac{4A}{P_W} = \frac{4\left[\delta\xi - \left((\pi/2-\theta)/\cos\theta - \tan\theta\right)\xi^2/4\right]}{2\delta+\xi} \tag{22}$$

where A [μm^2] is the cross-sectional area of wetting fluid (the rectangle's area minus the area of a circular segment) and P_W is the wetted perimeter (Hay et al., 2008). The fractal velocity v_f [mm/s] of water imbibition in fracture can be expressed as:

$$v_f = \frac{4Q}{\pi\lambda_f^2} = \frac{(1-\gamma)\lambda_f^2}{32\mu L_{ff}}\left[P_c + 2\Delta P_c - 2P_\mu\right] \tag{23}$$

where λ_f [μm] is the median fracture aperture, which can be calculated based on the fracture volume extracted from neutron radiography.

By substituting Eqs. (3), (19), (20), (21) into Eq. (23), the fractal velocity v_f [mm/s] can be expressed as:

$$v_f = \frac{(1-\gamma)\lambda_f^2}{32\mu L_{ff}}\left\{\frac{4\sigma\cos\theta}{\lambda_f} + \frac{2\sigma\left[(2\delta+\xi)\cos\theta - \xi\sin\theta\right]}{\delta\xi} - \frac{4P_0\mu L_{ff} v_f}{\tau_f d_h^2}\right\} \tag{24}$$

By substituting Eqs. (6), (7) into Eq. (24) yields:

$$\frac{dL_{sf}}{dt} = \frac{(1-\gamma)\tau_f\sigma\lambda_f^{2D_T-1}d_h^2\left[\left(2\delta\xi + 2\delta\lambda_f + \lambda_f\xi\right)\cos\theta - \lambda_f\xi\sin\theta\right]}{2\delta\xi\mu D_T L_{sf}^{2D_T-1}\left(8\tau_f d_h^2 + P_0\lambda_f^2\right)} \tag{25}$$

Integrating Eq. (25) under the initial condition $L_{sf}(0) = 0$ yields:

$$L_{sf} = \left\{\frac{(1-\gamma)\tau_f\sigma d_h^2\left[\left(2\delta\xi + 2\delta\lambda_f + \lambda_f\xi\right)\cos\theta - \lambda_f\xi\sin\theta\right]}{\delta\xi\mu\lambda_f^{1-1/\alpha}\left(8\tau_f d_h^2 + P_0\lambda_f^2\right)}\right\}^{\alpha} t^{\alpha} = C_f t^{\alpha} \tag{26}$$

where C_f [mm/s$^{\alpha}$] is the sorptivity of fracture, which can be expressed as:

$$C_f = \left\{\frac{(1-\gamma)\tau_f\sigma d_h^2\left[\left(2\delta\xi + 2\delta\lambda_f + \lambda_f\xi\right)\cos\theta - \lambda_f\xi\sin\theta\right]}{\delta\xi\mu\lambda_f^{1-1/\alpha}\left(8\tau_f d_h^2 + P_0\lambda_f^2\right)}\right\}^{\alpha} \tag{27}$$

Finally, the time exponent α of fracture can be calculated by

$$\alpha = \ln\left(\frac{C_f}{\lambda_f}\right) / \ln\left(\frac{(1-\gamma)\tau_f\sigma d_h^2\left[\left(2\delta\xi + 2\delta\lambda_f + \lambda_f\xi\right)\cos\theta - \lambda_f\xi\sin\theta\right]}{\delta\xi\mu\lambda_f\left(8\tau_f d_h^2 + P_0\lambda_f^2\right)}\right) \tag{28}$$

Based on this theoretical framework, Eqs. (27) and (28) can be used to predict the

sorptivity of rough-walled fracture in sandstone and the imbibition time exponent α of fracture in sandstone.

3 Materials and methods

3.1. Sandstone Specimen

The tested sandstone was collected from Rong County, Sichuan Province, China. The tested sandstone was prepared as a plate specimen, which was 41 mm × 10 mm × 35 mm in size and named as W1, as shown in Fig. 3(a). An artificial rough-walled fracture was then created on specimen W1 using the modified Brazilian test (Karpyn et al., 2009a), as shown in Fig. 3(b). Before the experiment, the sandstone specimen W1 was oven-dried at 105 °C until its weight was constant (Cheng et al., 2015). The sides of the specimen were wrapped in metal foil tape to prevent water wetting and evaporation (Zhao et al., 2017), as shown in Fig. 3(c). The microstructure of the rough-walled fracture surface was also obtained by using scanning electron microscopy (SEM) as shown in Fig. 3(d). The permeability K is 141 mD measured by using the chemically equilibrated water. Fig. 4 shows the PSD of a specimen based on mercury intrusion porosimetry (MIP). The porosity Φ is 19.50% and the majority of pores are concentrated in the range of 5-13 μm. Moreover, the mineral compositions of the sandstone were measured by using X-ray diffraction (XRD) and listed in Table 1. Clay minerals account for ~2.6% in the tested sandstone.

3.2. High-Resolution X-ray CT Imaging

A nanoVoxel-4000 high-resolution X-ray CT scanner (HRXCT) (SanYing Precision Instruments Co, Ltd., China) was used to investigate the pore and fracture structures of the specimen W1. The fractured structure of the specimen W1 was reconstructed and analysed by using image analysis software Avizo (FEI Co., USA). Fig. 5(a) shows the two-dimensional CT slice of the specimen. Fig. 5(b) shows the fracture volume of W1 extracted from HRXCT scanning. The count percent histogram distribution of fracture aperture in the sandstone specimen is shown in Fig. 5(c). A cylindrical sandstone specimen, drilled from the same sandstone block as specimen W1, with a diameter of 1.8mm was prepared for HRXCT scanning to better understand the pore

structure. The pore structure was also reconstructed and analysed by using Avizo. A volume of interest (VOI) of 600 × 600 × 600 voxels in the matrix of the sandstone was selected for further calculation of the pore structures, as shown in Fig. 6(a). Fig. 6(b) shows the two-dimensional CT slice of the VOI. The pore volumes need to be segmented from the matrix to calculate the porosity Φ, tortuosity. Based on the Otsu method, the Avizo Auto Thresholding module was used to calculate the recommended threshold of VOI (Zhao et al., 2017). In order to determine the optimum segmentation value of the sandstone specimen studied, the variation of porosity Φ under different threshold conditions were analysed, as listed in Table 2. The porosity Φ was calculated by using the Avizo quantification module (Zhao et al., 2017). By comparing the calculated porosity Φ with the measured porosity Φ by MIP, 1695 was set as the thresholds to segment the pore volumes in the VOI of the sandstone. The three-dimensional segmented pore volumes of VOI were showed in Fig. 6(c).

3.3. Neutron Radiography Setup

The imbibition experiments were performed at the cold-neutron guide B, located at the guide hall of China Advanced Research Reactor in the China Institute of Atomic Energy. The neutron flux rate was 1.03×10^7 n/cm^2/s when the reactor operated at a power of 20 MW (He et al., 2013). The neutron imaging facility is located next to the end of the beam guide, and the ratio of the collimator tube length to its aperture diameter is 85 (Zhao et al., 2018, 2017). The real-time detector system is equipped with a new generation CMOS sensor with 5.5 million pixels and speeds up to 100 fps at full frame (He et al., 2013).

The experiment was performed in the following three steps: (i) obtain 10 dark-current images (shutter closed, no neutron illumination) and 10 flat-field images (open shutter, without specimen) (Cheng et al., 2011); (ii) hang the specimen holder in front of the scintillator screen and fix specimen W1 on it, with the specimen 10 mm away from the scintillator screen; then, take 10 images of the dried specimen, denoted as $I_{(Dry)}$; and (iii) keep the shutter open and slowly lift an aluminium container filled with distilled water until the bottom of specimen W1 is in contact with the water surface—this moment is defined as the baseline (zero) time (Cheng et al., 2015).

Neutron images were obtained every 0.10 s to capture the rapid imbibition of water in fractured sandstone specimen and are denoted as wet reference image $I_{(Wet)}$. The experiment lasted 120 s and a total of 9 images were selected to show the rapid uptake of water into the fracture and enable us to calculate the sorptivity of fractured sandstone.

3.4. Neutron Image Processing

All the raw neutron radiographs were processed and analysed using the *ImageJ* software packages (Abràmofff et al., 2005; Schneider et al., 2012). For each acquired neutron image, the two-dimensional distribution of net water in the tested specimen can be obtained using the following steps (Zhao et al., 2017):

(i) One open-beam reference image, $I_{(OB)}$, one dark-field reference image, $I_{(DF)}$, and one dry reference image $I_{(Dry)}$ were acquired from the 10 dark-current images, 10 flat-field images, and 10 images of the dried specimen, respectively.

(ii) In order to remove background noise and beam heterogeneities in the detector and obtain the normalised image of the dry and wet sandstone, all raw neutron images of the dry and wet sandstone specimen were processed by using the following formula (Kang et al., 2014):

$$I_{nDry} = f_k \frac{I_{(Dry)} - I_{(DF)}}{I_{(OB)} - I_{(DF)}} \tag{29}$$

where I_{nDry} is the normalised image of the dry sandstone specimen and f_k is a rescaling factor used to correct for fluctuations in the neutron flux, which was taken as unity in this work because all the images were collected at the same power of the neutron beam. The normalised images of the wet sandstone specimen I_{nWet} can be obtained by replacing $I_{(Dry)}$ with $I_{(Wet)}$ in Eq. (29).

(iii) To remove the effect of the dry sandstone specimen and the aluminium foil tape on the neutron intensity and obtain the net-water transmission neutron images, we divided the normalised wet-specimen images I_{nWet} by the normalised images of the dry sandstone specimen I_{nDry} as (Kang et al., 2013):

$$I_w = \frac{I_{nWet}}{I_{nDry}} \tag{30}$$

where I_w denotes the net-water transmission neutron images. The selected net-water transmission images of specimen W1 are shown in Fig. 7.

The water thickness w_t [mm] penetrated by neutron beam in the specimen was calculated using the following expression (Kang et al., 2013):

$$w_t = -\frac{\zeta}{2\eta} - \sqrt{\left(\frac{\zeta}{2\eta}\right)^2 - \frac{1}{\eta}\ln\left(T_w\right)} \tag{31}$$

where T_w is the value of transmitted intensity, which changes only attribute to the variety of water content. The value of T_w is equal to the gray value extracted from the image I_w by using *ImageJ* software. ζ [mm^{-1}] is the attenuation coefficient for water, η [mm^{-2}] is the correction coefficient that takes into account beam hardening. The values of ζ and η were determined by calibration using water-filled Al cell machined to give a range of known water thicknesses, which is 0.4419 mm^{-1}and -0.0463 mm^{-2}, respectively (Zhao et al., 2018). Then, the volumetric water content θ_w can be calculated by

$$\theta_w = \frac{w_t}{L_w} \tag{32}$$

where L_w is the thickness of specimen penetrated by neutron beam.

3.5 Measurement of water wetting front

In order to quantify the evolution of the wetting front, several monitoring lines on the net-water transmission neutron images were set up to extract the change of the wetting front positions, as shown in Fig. 8. Considering the complexity of the microstructures in the tested sandstone, we superimposed 13 mm^2 red grids on the image to define 11 monitoring lines (including 9 vertical lines and 2 horizontal lines) to monitor the change of the water transmission with time. For instance, the blue lines show the No.2 and No.7 vertical monitoring lines in regions 1 and 2, the black lines show the No.10 and No.11 horizontal monitoring lines in regions 1 and 2 and the green line shows the No.9 vertical monitoring line in the fracture zone, as shown in Fig. 8(a). The distance travelled by the wetting front monitored by lines 2 (L_{m2}), 7 (L_{m7}), 9 (L_{sf}), 10 (H_{sm1}) and 11 (H_{sm2}) are shown in Fig. 8(a). The net-water transmission profiles along the vertical and horizontal direction of the specimen were

extracted from the image. The distribution of the transmissions along the No.2, No.7, No.9, No.10 and No.11 monitoring lines are shown in Fig. 8(b). The transmission increases in the direction of the water imbibition and where the value of the transmission is equal to or exceeds a threshold value, indicating a drying phase. The threshold value for specimen W1 is 0.95, based on the average transmission value of the dry image, as illustrated in Fig. 8(b). In this work, the specimen W1 is assumed not to be wetted by water when the average transmission exceeded the threshold value.

4. Results and Discussion

4.1. Evolution of Water Wetting Front

Fig. 7 shows the evolution of water imbibition in both the fracture zone and the matrix of the specimen W1 monitored by neutron radiography. The process of the evolution can be divided into three parts: (i) water imbibed into the matrix when the bottom of the specimen is in contact with water; (ii) then, water uptake rapidly into the fracture; (iii) last, water imbibed into the matrix from the fracture. The speed of water imbibition in the fracture is significantly larger than that in the matrix. The distance travelled by the wetting front in other monitoring lines (Nos. 1, 3, 4, 5, 6, 8) were measured, and the average distance L_{sm1} (in region 1) and L_{sm2} (in region 2) are obtained, as shown in Table 3.

In order to describe the wetting fronts in different regions of the specimen comparatively, the radiograph data obtained as t = 0.80 s (see Fig.8(a)) is taken as an example. It is found that the wetting front in the fracture reaches 34.77 mm, which is approximately 16 times larger than that in the matrix of region 1 (2.23 mm) or region 2 (2.05 mm). This phenomenon may be induced by the larger effective diameter of the fracture compared with that in the matrix, and the rougher surface of the fracture than that of the smooth capillary in the matrix. Cheng et al. (2015) believed that capillary dynamics could explain the more rapid uptake of water in a fracture than in the surrounding matrix during spontaneous imbibition. Moreover, water imbibed into the

matrix from the fracture is more rapid than that from the bottom of the specimen. H_{sm1} and H_{sm2} are 4.34 mm and 4.48 mm, which are approximate 2 times larger than the average value of L_{sm1} and L_{sm2}, as shown in Table 3. This result may be caused by two reasons. First, the fracture was produced by using the modified Brazilian method. The regions near the fracture may have more microcracks or damages. The width of the damaged zone varies between 2 and 10 times the width of the fracture aperture (Cheng et al., 2015). Second, there is no gravity effect for the horizontal evolution of the wetting front. Finally, the volumetric water content θ_w along the monitoring lines 10 and 11 are also calculated by using Eq. (32). The water loss coefficient γ can also be obtained by Eq. (17). Table 3 lists the average value $\bar{\theta}_w$ and the water loss coefficient γ at different imbibition time. The water loss coefficient γ rises with the increase of the imbibition time, except at time of 0.10 s. The boundary effect may cause this exception at 0.10 s. The average value of water loss coefficient γ is selected as one representative value to estimate the loss of water from the fracture to the matrix and as one of the important parameters to calculate the sorptivity of the fracture during the spontaneous imbibition.

4.2. Determination of Time Exponent

According to the literature review (Cheng et al., 2015; Kang et al., 2013; Zhao et al., 2017), the height of water imbibition in a matrix or fracture increases linearly with the square root of time (i.e., time exponent α = 0.50). However, these researches did not consider the uncertainty of the time exponent (i.e., $\alpha \neq 0.5$) caused by the heterogeneity of the medium or the capillary force disorder due to the randomness of pore sizes (Brú and Pastor, 2006; Cai and Yu, 2011). Fig. 9(a) shows that the wetting-front positions are monitored in both space and time. Quantitative results of the wetting-front position for each vertical and horizontal net-water transmission profile are obtained from the neutron radiographs. Fig. 9 presents that the double-logarithmic plots of the wetting-front positions versus time. The time exponent α can be estimated by using linear regression, and the values of goodness of fit (R^2) are larger than 0.93, as listed in Table 4. The results clearly show a

non-classical (i.e., time exponent $\alpha \neq 0.5$) behaviour of the wetting-front motion. The time exponent α for the wetting front motion in regions 1 and 2 of the matrix are 0.46 and 0.45 in the vertical direction and 0.33 and 0.40 in the horizontal direction, respectively. Possible causes of these variations are the randomness of the capillary force, which is related to the anisotropy of the medium and the randomness of the PSD (Brú and Pastor, 2006; Cai and Yu, 2011). Similar results have been reported for other porous medias (e.g., chalk, Bentonite clay, and Berea), with time exponent values of 0.40 for chalk (Li and Horne, 2004), 0.41 for Bentonite clay (Brú and Pastor, 2006), and 0.32 for Berea sandstone (Li et al., 2006). Moreover, it can be seen the first points of some of the data sets tends to slight deviation from the best fit line in Fig. 9. These deviations may be caused by the effect of boundary that affects the rate of spontaneous imbibition (Yildiz et al., 2006). Moreover, the existence of the boundary will affect the equipotential line distribution of the imbibition field and the streamline distribution.

4.3. Sorptivity Analysis

4.3.1 Sorptivity from Nonlinear regression of the experimental data

Fig. 10 shows the relationships of the wetting-front position in the matrix and the fracture with the time. The sorptivity of the sandstone matrix C_m (regions 1 and 2) and the fracture C_f can be estimated by the nonlinear regression of the plotted points. It is found that the first point of the data set of fracture (see Fig. 10(a)) tends to fall below the fitting line. Possible causes of this deviations are: (i) the bottom of the specimen may not have been perfectly aligned with the water surface resulting in partial contact at very early times, and (ii) the first image is integrated over a relatively long period of time (5–10 ms) relative to the rate of wetting at very early times (Cheng et al., 2015).

Table 5 presents the sorptivities of the matrix (C_m) and the fracture zone (C_f) obtained by experimental fit, and all the values of the goodness of fit (R^2) are larger than 0.96. It is found that the sorptivity of the fracture is 39.61 mm/s$^{0.38}$. Cheng et al. (2015) reported that the fracture sorptivity of Berea sandstone ranges from 17.87 to

27.12 mm/s$^{0.50}$ by linear regression of the experimental data. However, most of the previous studies on the sorptivity of rocks regard the time exponent α as 0.50 (Cheng et al., 2015; Hammecker and Jeannette, 1994; Hassanein et al., 2006; Zhao et al., 2017). In the current study, the time exponent is 0.38 for the fracture sorpotivity. The matrix sorptivities near the bottom of the specimen are 2.33 mm/s$^{0.46}$ (region 1) and 2.18 mm/s$^{0.45}$ (region 2). But the values of sorptivities near the fracture damage zone are 4.42 mm/s$^{0.33}$ (line 10) and 4.93 mm/s$^{0.40}$ (line 11), which are approximately 2 times larger than that near the bottom of the specimen. This result quantifies the difference between the imbibition rate of water from the fracture or the bottom of the specimen into the matrix. The matrix sorptivity near the bottom of the specimen obtained by nonlinear regression is basically consistent in regions 1 and 2, regardless of the values of the time exponent α. The slight variations of the sorptivity in the matrix may be caused by the heterogeneity of the tested sandstone and the shrinkage, closure, and elimination of pore throats during the imbibition process (Benavente et al., 2015; Zhao et al., 2017). Moreover, the sorptivity of the fracture obtained by nonlinear regression is much larger than that of the matrix. This may be caused by not only the capillary uptake within the fracture aperture but also by the surface spreading of water on the side walls of the fracture (Cheng et al., 2015). Nevertheless, the increased micro-crack density associated with localised damage near the fracture may enhance the sorption of fracture (Hall, 2013). Sahmaran and Li (2009) and Zhang et al. (2010a) also observed the enhanced sorption phenomenon in fractured cementitious materials. The above results not only prove that the fracture can significantly increase imbibition in fractured sandstone, but also show the heterogeneity effects on the sorptivity.

4.3.2 Sorptivity from Model Prediction

In this section, we employ fractal models (Eqs. (15) and (27)) to predict the sorptivity for both the matrix and the fracture of tested sandstone. The parameters used to calculate the sorptivity are listed in Table 6. The value of δ is equal to the average sand grain diameter of specimen W1, which is obtained by measuring the SEM image of the fracture surface (see Fig. 3(d)) using ImageJ software. The average

sand grain diameter of specimen W1 is 193.52 μm, which is consistent with the normal particle size range of sandstone (i.e., 125 to 250 μm) reported by Folk (1980). Fig. 5(a) was imported into AutoCAD software, and the fracture was depicted by using the polyline. The tortuous and the straight-line length of the fracture was measured, and the τ_f can be calculated to be 1.05. The aperture of the rough-walled fracture is calculated based on the three-dimensional fracture volume obtained by HRXCT (see Fig. 5(b)). The calculated results showed the fracture aperture varied from 7.7 to 770.30 μm, as shown in Fig. 5(c). Thus, the median aperture λ_f is 389 μm. The two-dimensional fractal dimension of pores D equals to 1.84, which is measured by using Fractal Box counter in ImageJ software based on two-dimensional CT slice of the specimen (see Fig. 6(b)). The tortuosity of pore structure τ is calculated by Avizo centroid path tortuosity module base on the pore structure data of VOI after segmentation and equals to 2.06 (see Fig. 6(c)). The value of λ_{max} is calculated by using Eq. (14) and equals to 22.76 μm. The average value of water loss coefficient γ in Table 3 equals to 0.28, which is used in the sorptivity calculation. Feng et al. (2004) reported that the value of β range from 10^{-4} to 10^{-2} in porous media. Take region 1 as an example, we analyzed the effect of β with the values of 10^{-4}, 10^{-3} and 10^{-2} on the prediction of matrix sorptivity. The predicted results of the matrix sorptivity (region 1) are 0.20 mm/s$^{0.46}$, 0.70 mm/s$^{0.46}$ and 2.41 mm/s$^{0.46}$ corresponding to the β of 10^{-4}, 10^{-3} and 10^{-2}. Based on the experimental nonlinear fitting values of the matrix sorptivity (region 1), when β equals to 10^{-4} or 10^{-3}, the predicted values of the developed model significantly underestimate the sorptivity of matrix. When $\beta = 10^{-2}$, the value of the matrix sorptivity predicted by the developed model is close to the experimental nonlinear fitting value. Moreover, Cai et al. (2010b) suggested that the minimum pore diameter λ_{min} is usually two orders of magnitude smaller than the maximum pore diameter λ_{max}. Based on the experimental data regression, β of 10^{-2} was chosen because it gave the best modeled results. Table 7 shows the sorptivities of various regions in the sandstone predicted by experimental nonlinear fitting and developed model, comparatively. The matrix sorptivities near the bottom of the specimen obtained by the model prediction are 1.03 (region 1) and 1.07 (region 2) times larger

than the values obtained by nonlinear regression. These results prove that the sorptivity of the matrix (surrounding the fracture) can be interpreted from the model. Some deviation of the model predicted sorptivity to the experimental fitting result may be caused by the following issues: (i) some infilling materials (such as clay minerals and quartz grains) within the pores reduce the effective seepage radius of the pores; (ii) the connectivity of the pores may be reduced due to the expansion of the clay mineral (such as illite and kaolinite) in contact with water (Zhao et al., 2017). Table 7 also indicates that the matrix sorptivities near the fracture damage zone obtained by the model prediction are seriously underestimated. It is caused by the underestimated porosity value used in the model. As mentioned in the previous Sections, the fracture of the tested sandstone was manufactured by the modified Brazil test method, which could induce damage of the regions near the fracture. These damage and microcracks close to the fracture will increase the sorption ability of the matrix (Cheng et al., 2015; Hall et al., 2013). The fracture sorptivity predicted by Eq. (27) is 1.04 times larger than the value obtained by nonlinear regression. Many previous studies related to the water flow in the fracture are based on the assumption of one-dimensional flow, which means no water will loss or imbibe from the fracture into the matrix (Andersen et al., 2018a; Cheng et al., 2015). If we do not consider the water loss coefficient in Eq. (30), the predicted fracture sorptivity is 45.67 mm/s$^{0.38}$, which is 1.15 times larger than the value obtained by nonlinear regression of experimental data. Thus, the error of predicted fracture sorptivity is approximate 15% for the tested sandstone by using one dimensional assumption, but the error of our developed model of fracture sorptivity is just ~4%. Eq. (27) considers the actual situation of water from the fracture to the matrix during the spontaneous imbibition of water in the fracture of sandstone, which cause the predicted fracture sorptivity is closer to the actual value. These results prove that the developed sorptivity model of fracture (Eq. (27)) is more effective. Moreover, neutron radiography provides an effective tool to obtain the basic data to calculate the water loss coefficient. It needs to point that the imbibition time exponent α of fracture in the tested sandstone equals to 0.38 by using Eq. (28). This value is consistent with that obtained by linear regression

of experimental data. It also indicates that Eq. (28) is effective and provides a new method to estimate the time exponent of water imbibed into rough-walled fractures in sandstone.

All of the above results may provide a better understanding of the sorptivity in matrix and fracture of sandstone. However, further studies are also necessary to evaluate the validity of the models for other rocks. The applicability of the models developed based on the laboratory scale test to the in-situ test also needs to be verified.

5. Summary and Conclusion

In this study, the dynamics of water imbibition in the unsaturated fractured sandstone is monitored successfully by neutron radiography. The wetting front in the fracture moves faster than that in the matrix. Moreover, the dynamic evolution of the wetting front in both the matrix and the fracture do not obey the L-W equation, with the time component $\alpha \neq 0.5$. Experimental results show that the wetting front advanced linearly with the power α of the time. The sorptivity of matrix and fracture were estimated by nonlinear regression of the experimental data. A fractal model is further modified to predict the sorptivity of the matrix, which takes into account the fractal dimension of tortuosity. A new fractal model is established to predict the sorptivity of a rough-walled fracture in the unsaturated sandstone, which considers the water losses from the fracture to the matrix. By comparing the experimental and model prediction results, we found that (i) the maximum pore size, pore fractal dimension and the fractal dimension of the tortuosity have a major influence on the determination of the sorptivity of matrix; (ii) the fracture aperture, the tortuosity of fracture, the fractal dimension of tortuosity, water losses coefficient and the diameter of sandstone particle play an important role in the prediction of fracture sorptivity. Moreover, the established fractal model also provides a new method to estimate the imbibition time exponent of fracture. This work provides important findings and guidance to further investigate this phenomenon in other natural and engineered porous media. This phenomenon is likely to be particularly important in engineering applications, such as

the exploitation of unconventional gas resources (e.g., sandstone/shale gas) by using hydraulic fracturing. However, some limitations are worth noting. In this study, we assumed the imbibition channel in the matrix as tortuous capillary tubes, without considering the intersections of parallel capillaries. Moreover, the current theoretical framework represents an only approximation of imbibition behaviour within the unsaturated fractured sandstone used in this work. Thus, more types of specimens need to be studied.

Acknowledgments

The results presented in this article rely on the data collected at the Neutron Scattering Laboratory, China Institute of Atomic Energy. The China Institute of Atomic Energy is gratefully acknowledged for their support of this work and for providing access to the neutron imaging facility. This research is supported by the National Key R&D Program of China (2016YFC0600708, 2016YFA0401502 and 2016YFC0801401), National Natural Science Foundation of China (No. 51874312, 51861145403), Open Project Program of State Key Laboratory of Water Resource Protection and Utilization in Coal Mining (SHJT-16-30.17), Yue Qi Distinguished Scholar Project of China University of Mining & Technology (Beijing), Fundamental Research Funds for the Central Universities.

References

Abràmofff, M.D., Magalhães, P.J., Ram, S.J., 2005. Image processing with ImageJ Part II. Biophotonics International 11, 36–43. https://doi.org/10.1117/1.3589100

Andersen, P.Ø., Brattekås, B., Nødland, O., Lohne, A., Føyen, T.L., Fernø, M.A., 2018a. Darcy-Scale Simulation of Boundary-Condition Effects During Capillary-Dominated Flow in High-Permeability Systems. SPE Reservoir Evaluation & Engineering 1–19. https://doi.org/https://doi.org/10.2118/188625-PA

Andersen, P.Ø., Lohne, A., Stavland, A., Hiorth, A., Brattekås, B., 2018b. Core Scale Simulation of Spontaneous Solvent Imbibition from HPAM Gel, in: SPE Improved Oil Recovery Conference. Tulsa, Oklahoma, USA.

Aydin, A., 2000. Fractures,faults,and hydrocarbon entrapment, migration and flow. Marine and Petroleum Geology 17.

Balankin, A.S., Susarrey, O., 2003. Scaling Properties of Pinned Interfaces in Fractal Media. Physical Review Letters 90, 096101. https://doi.org/10.1103/PhysRevLett.90.096101

Bear, J., 1972. Dynamics of fluids in porous media. Engineering Geology 7, 174–175.

Benavente, D., Lock, P., Ángeles, M., Del, G., 2002. Predicting the Capillary Imbibition of Porous Rocks from Microstructure. Transport in Porous Media 49, 59–76.

Benavente, D., Pla, C., Cueto, N., Galvañ, S., Martínez-Martínez, J., García-del-Cura, M.A., Ordóñez, S., 2015. Predicting water permeability in sedimentary rocks from capillary imbibition and pore structure. Engineering Geology 195, 301–311. https://doi.org/10.1016/j.enggeo.2015.06.003

Bodvarsson, G.S., W.Boyle, R.Patterson, D.Williams, 1999. Overview of scientific investigations at Yucca Mountain-the potential repository for high-level nuclear waste. Journal of Contaminant Hydrology 38, 3–24.

Brú, A., Pastor, J.M., 2006. Experimental characterization of hydration and pinning in bentonite clay, a swelling, heterogeneous, porous medium. Geoderma 134, 295–305. https://doi.org/10.1016/j.geoderma.2006.03.006

Cai, J., Perfect, E., Cheng, C., Hu, X., 2014. Generalized Modeling of Spontaneous Imbibition Based on Hagen-Poiseuille Flow in Tortuous Capillaries with Variably Shaped Apertures. Langmuir 30, 5142–5151. https://doi.org/10.1021/la5007204

Cai, J., Yu, B., 2011. A Discussion of the Effect of Tortuosity on the Capillary Imbibition in Porous Media. Transport in Porous Media 89, 251–263. https://doi.org/10.1007/s11242-011-9767-0

Cai, J., Yu, B., Mei, M., Luo, L., 2010a. Capillary rise in a single tortuous capillary. Chinese Physics Letters 27, 1–4. https://doi.org/10.1088/0256-307X/27/5/054701

Cai, J., Yu, B., Zou, M., Luo, L., 2010b. Fractal characterization of spontaneous co-current imbibition in porous media. Energy and Fuels 24, 1860–1867. https://doi.org/10.1021/ef901413p

Cheng, C.L., Kang, M., Perfect, E., Voisin, S., Horita, J., Bilheux, H.Z., Warren, J.M., Jacobson, D.L., Hussey, D.S., 2011. Average Soil Water Retention Curves Measured by Neutron Radiography. Soil Science Society of America Journal 76, 1184–1191. https://doi.org/10.2136/sssaj2011.0313

Cheng, C.L., Perfect, E., Donnelly, B., Bilheux, H.Z., Tremsin, A.S., McKay, L.D., DiStefano, V.H., Cai, J.C., Santodonato, L.J., 2015. Rapid imbibition of water in fractures within unsaturated sedimentary rock. Advances in Water Resources 77, 82–89. https://doi.org/10.1016/j.advwatres.2015.01.010

Cnudde, V., Dierick, M., Vlassenbroeck, J., Masschaele, B., Lehmann, E., Jacobs, P., Van Hoorebeke, L., 2008. High-speed neutron radiography for monitoring the water absorption by capillarity in porous materials. Nuclear Instruments and Methods in Physics Research, Section B: Beam Interactions with Materials and Atoms 266, 155–163. https://doi.org/10.1016/j.nimb.2007.10.030

Czachor, A., El-Ghany El-Abd, A., Milczarek, J.J., 2002. Determination of Capillary Motion of Water in Bricks Using Neutron Radiography. Acta Physica Polonica A 102, 245–252. https://doi.org/10.12693/APhysPolA.102.245

Daniel, T.B., Harihar, R., David, D., Hari, S.V., 2015. Hydraulic fracturing fluid migration in the subsurface: A review and expanded modeling results. Water Resources Research 7159–7188. https://doi.org/10.1002/2015WR017810.Received

Dewanckele, J., Kock, T. De, Fronteau, G., Derluyn, H., Vontobel, P., Dierick, M., 2013. Neutron radiography and X-ray computed tomography for quantifying weathering and water uptake processes inside porous limestone used as building material. Materials Characterization 88, 86–99. https://doi.org/10.1016/j.matchar.2013.12.007

Doster, F., Nordbotten, J.M., Celia, M.A., 2013. Impact of capillary hysteresis and trapping on vertically integrated models for CO2 storage. Advances in Water Resources 62, 465–474.

https://doi.org/10.1016/j.advwatres.2013.09.005

El Abd, A.E.-G., Czachor, A., Milczarek, J.J., 2009. Neutron radiography determination of water diffusivity in fired clay brick. Applied Radiation and Isotopes 67, 556–559. https://doi.org/10.1016/j.apradiso.2008.11.014

Faybishenko, B., Witherspoon, P.A., Bodvarsson, S., 2005. Emerging Issues in Fractured-Rock Flow and Transport Investigations : Introduction and Overview, American Geophysical Union.

Feng, Y., Yu, B., Zou, M., Zhang, D., 2004. A generalized model for the effective thermal conductivity of porous media based on self-similarity. Journal of Physics D: Applied Physics 37, 3030–3040. https://doi.org/10.1088/0022-3727/37/21/014

Folk, R.L., 1980. Petrology of sedimentary rocks. Hemphill Publishing Co., Austin, Texas, pp. 3–5.

Hall, S.A., 2013. Characterization of fluid flow in a shear band in porous rock using neutron radiography neutron radiography. Geophysical Research Letters 40, 2613–2618. https://doi.org/10.1002/grl.50528

Hammecker, C., Barbiero, L., Boivin, P., 2004. A Geometrical Pore Model for Estimating the Microscopical Pore Geometry of Soil with Infiltration Measurements. Transactions of the Society of Rheology 54, 193–219. https://doi.org/10.1023/A

Hammecker, C., Jeannette, D., 1994. Modelling the capillary imbibition kinetics in sedimentary rocks: Role of petrographical features. Transport in Porous Media 17, 285–303. https://doi.org/10.1007/BF00613588

Hassanein, R., Meyer, H.O., Carminati, A., Estermann, M., Lehmann, E., Vontobel, P., 2006. Investigation of water imbibition in porous stone by thermal neutron radiography. Journal of Physics D: Applied Physics 39, 4284–4291. https://doi.org/10.1088/0022-3727/39/19/023

Hay, K.M., Dragila, M.I., 2008. Physics of fluid spreading on rough surfaces. International Journal of Numerical Analysis and Modeling 5, 85–92.

Hay, K.M., Dragila, M.I., Liburdy, J., 2008. Theoretical model for the wetting of a rough surface. Journal of Colloid and Interface Science 325, 472–477. https://doi.org/10.1016/j.jcis.2008.06.004

He, L., Han, S., Wang, H., Hao, L., Wu, M., Wei, G., Wang, Y., Liu, Y., Sun, K., Chen, D., 2013. Design of real-time neutron radiography at China Advanced Research Reactor. Physics Procedia 43, 48–53. https://doi.org/10.1016/j.phpro.2013.03.006

Herring, A.L., Harper, E.J., Andersson, L., Sheppard, A., Bay, B.K., Wildenschild, D., 2013. Effect of fluid topology on residual nonwetting phase trapping: Implications for geologic CO2 sequestration. Advances in Water Resources 62, 47–58. https://doi.org/10.1016/j.advwatres.2013.09.015

Hunt, J.R., Tompson, A.F.B., 2005. Tracing long-term vadose zone processes at the Nevada Test Site, USA. Hydrol Process . 19(17): 3383–3394. https://doi.org/10.1007/s11103-011-9767-z.Plastid

Joekar-Niasar, V., Prodanovi, M., Wildenschild, D., Hassanizadeh, S.M., 2010. Network model investigation of interfacial area,capillary pressure and saturation relationships in granular porous media. Water Resour Res. 46, 1–18. https://doi.org/10.1029/2009WR008585

Kang, M., Perfect, E., Cheng, C.L., Bilheux, H.Z., Gragg, M., Wright, D.M., Lamanna, J.M., Horita, J., Warren, J.M., 2013. Diffusivity and Sorpvity of Berea Sandstone Determined using Neutron Radiography. Vadose Zone Journal 12, 1712–1717. https://doi.org/10.2136/vzj2012.0135

Kang, M., Perfect, E., Cheng, C.L., Bilheux, H.Z., Lee, J., Horita, J., Warren, J.M., 2014. Multiple pixel-scale soil water retention curves quantified by neutron radiography. Advances in Water Resources 65, 1–8. https://doi.org/10.1016/j.advwatres.2013.12.004

Karoglou, M., Moropoulou, A., Giakoumaki, A., Krokida, M.K., 2005. Capillary rise kinetics of some building materials. Journal of Colloid and Interface Science 284, 260–264. https://doi.org/10.1016/j.jcis.2004.09.065

Karpyn, Z.T., Alajmi, A., Radaelli, F., Halleck, P.M., Grader, A.S., 2009a. X-ray CT and hydraulic evidence for a relationship between fracture conductivity and adjacent matrix porosity. Engineering Geology 103, 139–145. https://doi.org/10.1016/j.enggeo.2008.06.017

Karpyn, Z.T., Halleck, P.M., Grader, A.S., 2009b. An experimental study of spontaneous imbibition in fractured sandstone with contrasting sedimentary layers. Journal of Petroleum Science and Engineering 67, 48–56. https://doi.org/10.1016/j.petrol.2009.02.014

Katz, A.J., Thompson, A.H., 1985. Fractal Sandstone Pores:Implications for Conductivity and Pore Formation. Physical Review Letters 54, 1325–1328.

Krohn, E., 1988. Fractal Measurements of Sandstones, Shales, and Carbonates. Journal of Geophysical Research 93, 3297–3305.

Laughlin, R.D., Davies, J.E., 1961. Some Aspects of Capillary Absorption in Fibrous Textile Wicking. Textile Research Journal 31, 904–910. https://doi.org/10.1177/004051756103101011

Leventis, A., Verganelakis, D.A., Halse, M.R., Webber, J.B., 2000. Capillary Imbibition and Pore Characterisation in Cement Pastes. Transport in Porous Media 39, 143–157.

Li, K., Horne, R., 2001. Characterization of Spontaneous Water Imbibition Into Gas-Saturated Rocks. SPE Journal 6, 1–12. https://doi.org/10.2118/74703-PA

Li, K., Horne, R.N., 2004. An Analytical Scaling Method for Spontaneous Imbibition in Gas-Water-Rock Systems. SPE Journal 9(3), 322–329.

Li, K., Stanford, U., Peking, U., Chow, K., Horne, R.N., Stanford, U., 2006. Influence of Initial Water Saturation on Recovery by Spontaneous Imbibition in Gas / Water / Rock Systems and the Calculation of Relative Permeability. SPE Reservoir Evaluation & Engineering 9, 295–301.

Li, K., Zhao, H., 2012. Fractal Prediction Model of Spontaneous Imbibition Rate. Transport in Porous Media 91, 363–376. https://doi.org/10.1007/s11242-011-9848-0

Lucas, R., 1918. Rate of capillary ascension of liquids. Kolloid Z 23, 15–22.

Sahmaran, M., Li, V., 2009. Influence of microcracking on water absorption and sorptivity of ECC. Materials and Structures 42, 593–603. https://doi.org/10.1617/s11527-008-9406-6

Schneider, C.A., Rasband, W.S., Eliceiri, K.W., 2012. NIH Image to ImageJ: 25 years of image analysis. Nature Methods 9, 671–675. https://doi.org/10.1038/nmeth.2089

Serhat, A., Kovscek, A.R., 1999. Imbibition Studies of Low-Permeability Porous Media. SPE Journal 26–27. https://doi.org/10.2118/54590-MS

Tompson, A.F.B., Hudson, G.B., Smith, D.K., Hunt, J.R., 2006. Analysis of radionuclide migration through a 200-m Vadose zone following a 16-year infiltration event. Advances in Water Resources 29, 281–292. https://doi.org/10.1016/j.advwatres.2005.02.015

Washburn, E.W., 1921. The dynamics of capillary flow. Physical Review 17, 273–283.

Wheatcraft, S.W., Tyler, S.W., 1988. An Explanation of Scale-Dependent Dispersivity in Heterogeneous Aquifers Using Concepts of Fractal Geometry. Water Resour Res. 24, 566–578.

Yildiz, H.O., Gokmen, M., Cesur, Y., 2006. Effect of shape factor, characteristic length, and boundary conditions on spontaneous imbibition. Journal of Petroleum Science and Engineering 53, 158–170. https://doi.org/10.1016/j.petrol.2006.06.002

Yu, B., 2008. Analysis of Flow in Fractal Porous Media. Applied Mechanics Reviews 61, 1239–1249. https://doi.org/10.1115/1.2955849

Yu, B., 2005. Fractal character for tortuous streamtubes in porous media. Chinese Physics Letters 22, 158–160.

Yu, B., Cheng, P., 2002. A Fractal Permeability Model for Bi- Dispersed Porous Media. International Journal of Heat and Mass Transfer 45, 2983–2993. https://doi.org/10.1016/S0017-9310(02)00014-5

Yu, B., Li, J., 2001. Some fractal characters of porous media. Fractals 9, 365–372. https://doi.org/10.1115/1.2955849

Yu, B., Xu, P., Cai, J., Yun, M.-J., 2008. Fractal Analysis of Power-Law Fluid in a Single Capillary. Chinese Physics Letters 25, 616–619. https://doi.org/10.1088/0256-307X/25/2/071

Zhang, P., Wittmann, F.H., Zhao, T., Lehmann, E., 2009. Observation of Water Penetration of water into uncracked and cracked steel Reinforced Concrete Elements by Means of Neutron Radiography. Journal of Qingdao Technological University 29, 10–16.

Zhang, P., Wittmann, F.H., Zhao, T., Lehmann, E.H., 2010a. Neutron imaging of water penetration into cracked steel reinforced concrete. Physica B: Condensed Matter 405, 1866–1871. https://doi.org/10.1016/j.physb.2010.01.065

Zhang, P., Wittmann, F.H., Zhao, T., Lehmann, E.H., Vontobel, P., 2011. Neutron radiography,a powerful method to determine time-dependent moisture distributions in concrete. Nuclear Engineering and Design 241, 4758–4766. https://doi.org/10.1016/j.nucengdes.2011.02.031

Zhang, P., Wittmann, F.H., Zhao, T.J., Lehmann, E.H., Tian, L., Vontobel, P., 2010b. Observation and quantification of water penetration into Strain Hardening Cement-based Composites (SHCC) with multiple cracks by means of neutron radiography. Nuclear Instruments and Methods in Physics Research A 620, 414–420. https://doi.org/10.1016/j.nima.2010.04.119

Zhao, Y., Xue, S., Han, S., Chen, Z., Liu, S., Elsworth, D., He, L., Cai, J., Liu, Y., Chen, D., 2017. Effects of microstructure on water imbibition in sandstones using X-ray computed tomography and neutron radiography. Journal of Geophysical Research :Solid Earth 122, 4963–4981. https://doi.org/10.1002/2016JB013786

Zhao, Y., Xue, S., Han, S., He, L., Chen, Z., 2018. Characterization of unsaturated diffusivity of tight sandstones using neutron radiography. International Journal of Heat and Mass Transfer 124, 693–705. https://doi.org/10.1016/j.ijheatmasstransfer.2018.03.090

List of Figures

Fig. 9. The log–log plot of the wetting front position versus time in the matrix near the bottom and the fracture zone (a), and the matrix near the fracture (b) of specimen W1.

Fig. 10. Wetting front position versus the power α of the time for the matrix near the bottom and fracture (a), the matrix near the fracture (b) in specimen W1 measured using dynamic neutron radiography.

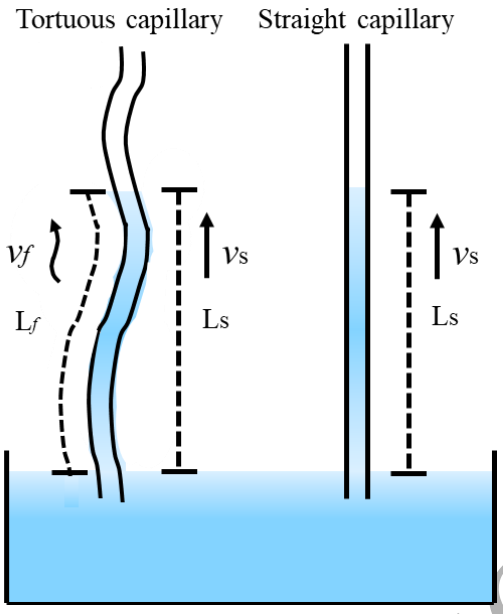

Fig. 1. The schematic of water imbibition in tortuous or straight capillary tube.

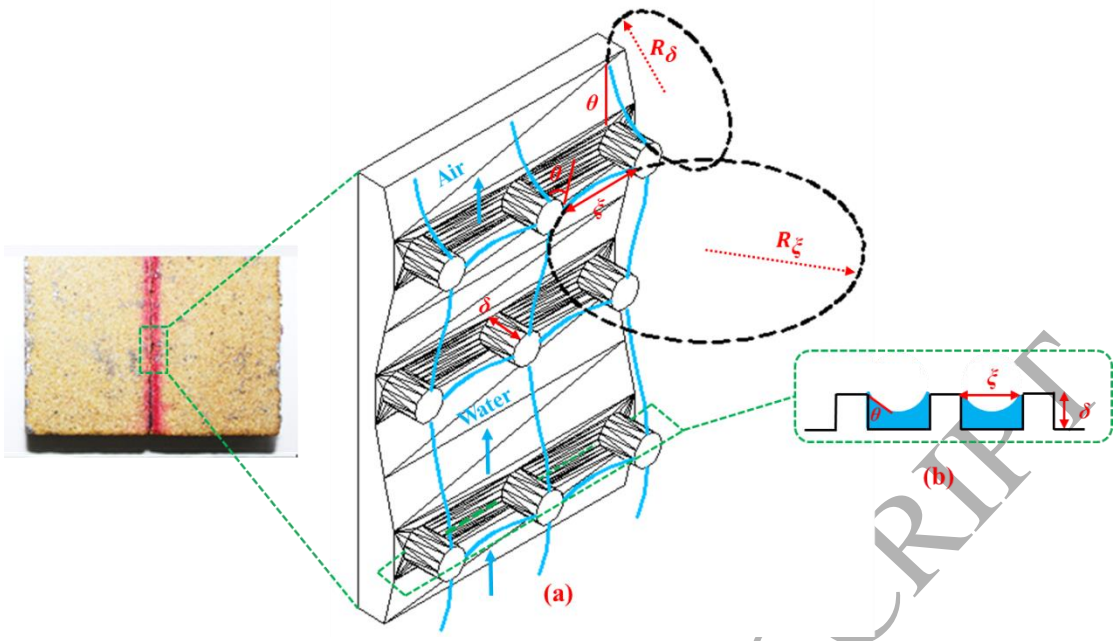

Fig. 2. Illustration of the air-water interface created by the presence of roughness. All air–water–solid contact angles θ are identical. Interface curvature creates capillarity and drives flow. The direction of water movement is shown by the arrow. Determination of the radius of curvature is governed by ξ and δ. (a) The modified geometric model for surface roughness proposed in this paper (idealized as the rough surface consists of a series of small cylinders arranged on a curved smooth surface). (b) The cross section schematic diagram of the model.

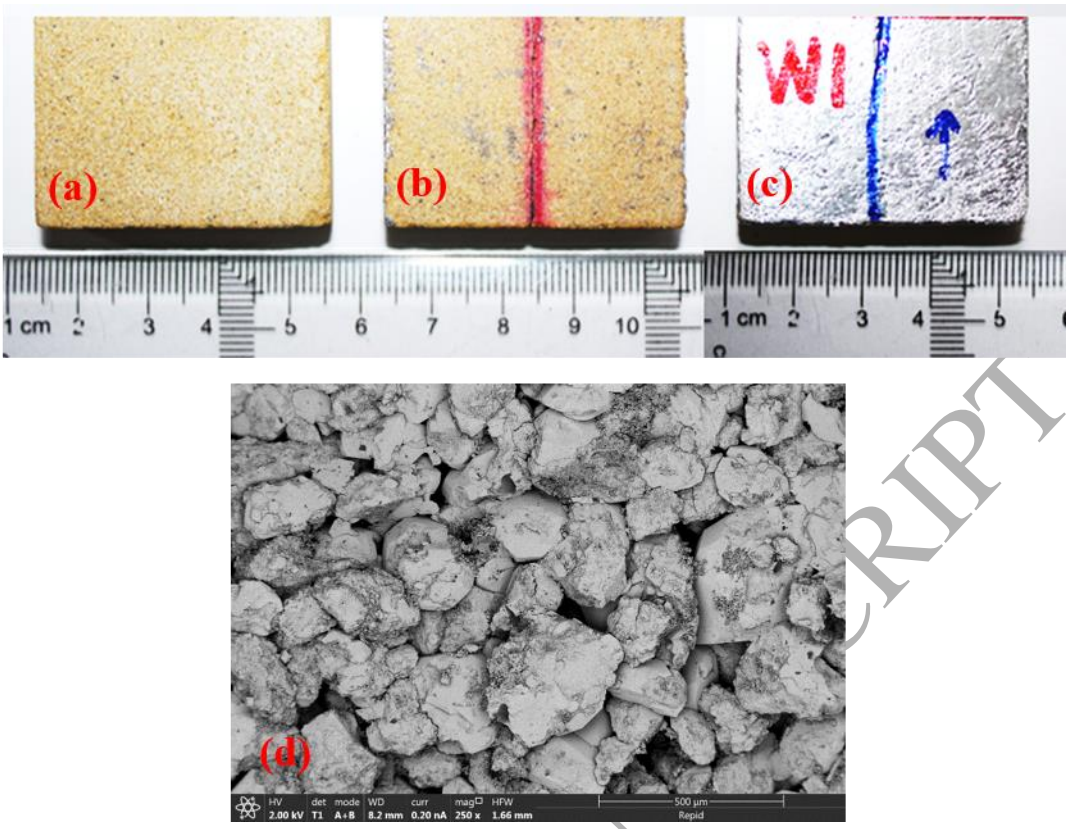

Fig. 3. Specimen investigated in the imbibition test. (a) The specimen is a fine sandstone named W1. (b) The fractured specimen obtained by using modified Brazilian test. (c) The fractured specimen was wrapped by metal foil tape to prevent water wetting and evaporation. (d) The microstructure of the rough-walled fracture surface was obtained by SEM.

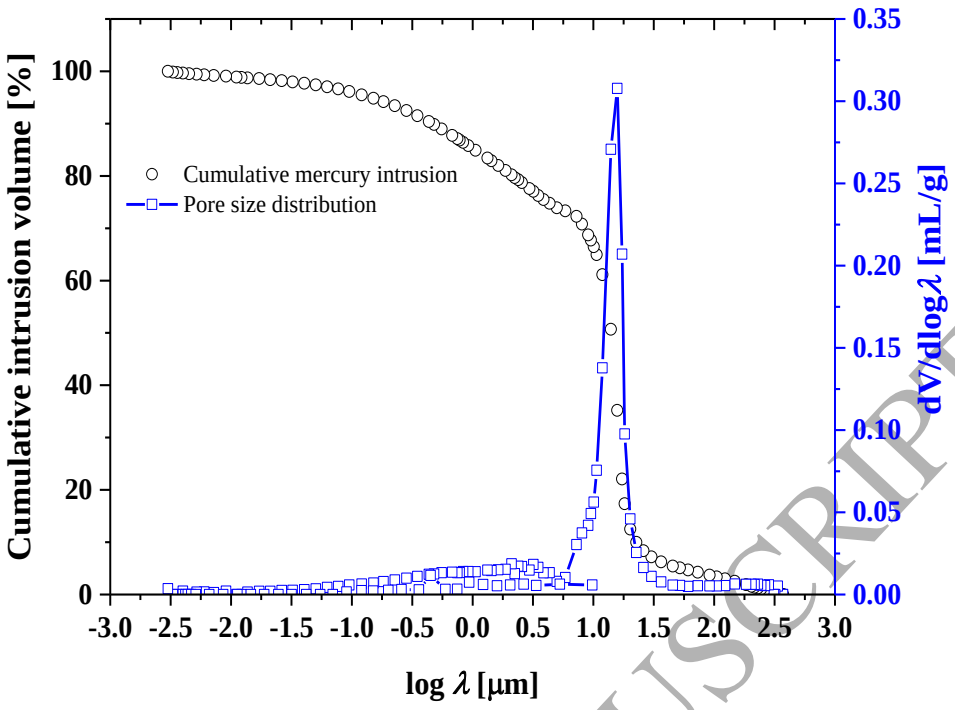

Fig. 4. Results of MIP experiment for the specimen W1. Cumulative mercury intrusion and pore size distribution curve of sandstone. Here dV/d(logλ) is the log differential intrusion versus diameter.

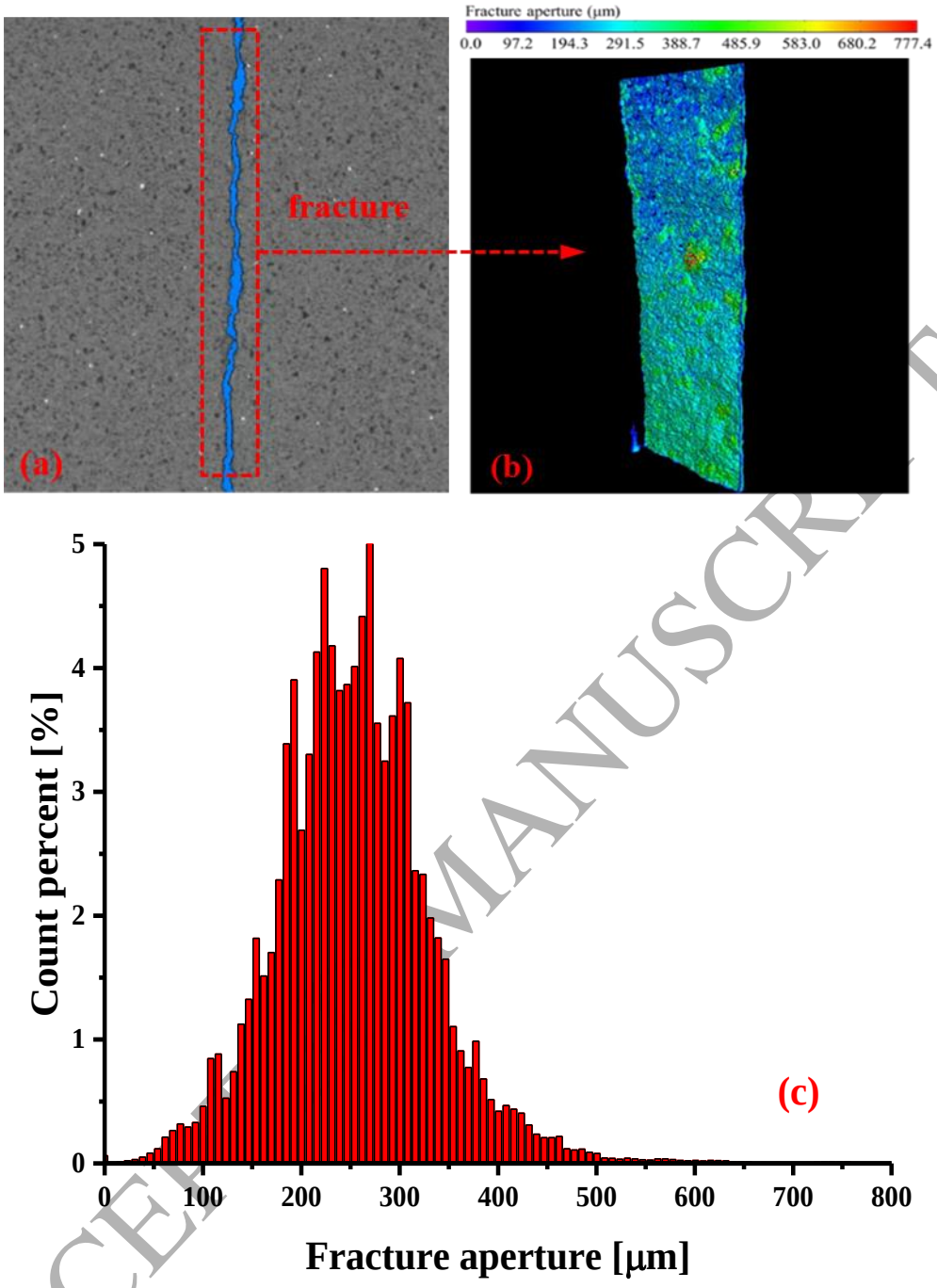

Fig. 5. Reconstruction of the fracture and matrix in sandstone specimen. (a) The two-dimensional CT slice of the specimen. (b) The three-dimensional Fracture aperture map. (c) The count percent histogram distribution of fracture aperture in sandstone specimen.

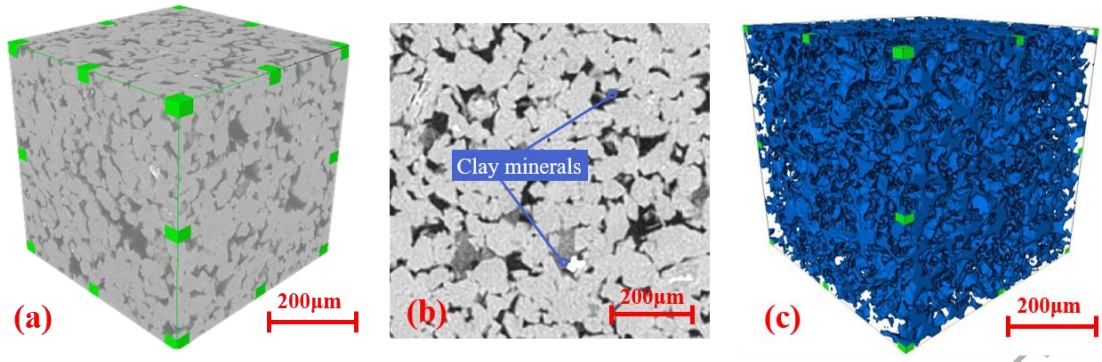

Fig. 6. Reconstruction of the fracture and matrix in sandstone specimen. (a) A volume of interest (VOI) of 600 × 600 × 600 voxels selected from the matrix of the sandstone. (b) The two-dimensional CT slice of the VOI in matrix of sandstone. (c) The three-dimensional segmented pore volumes of VOI.

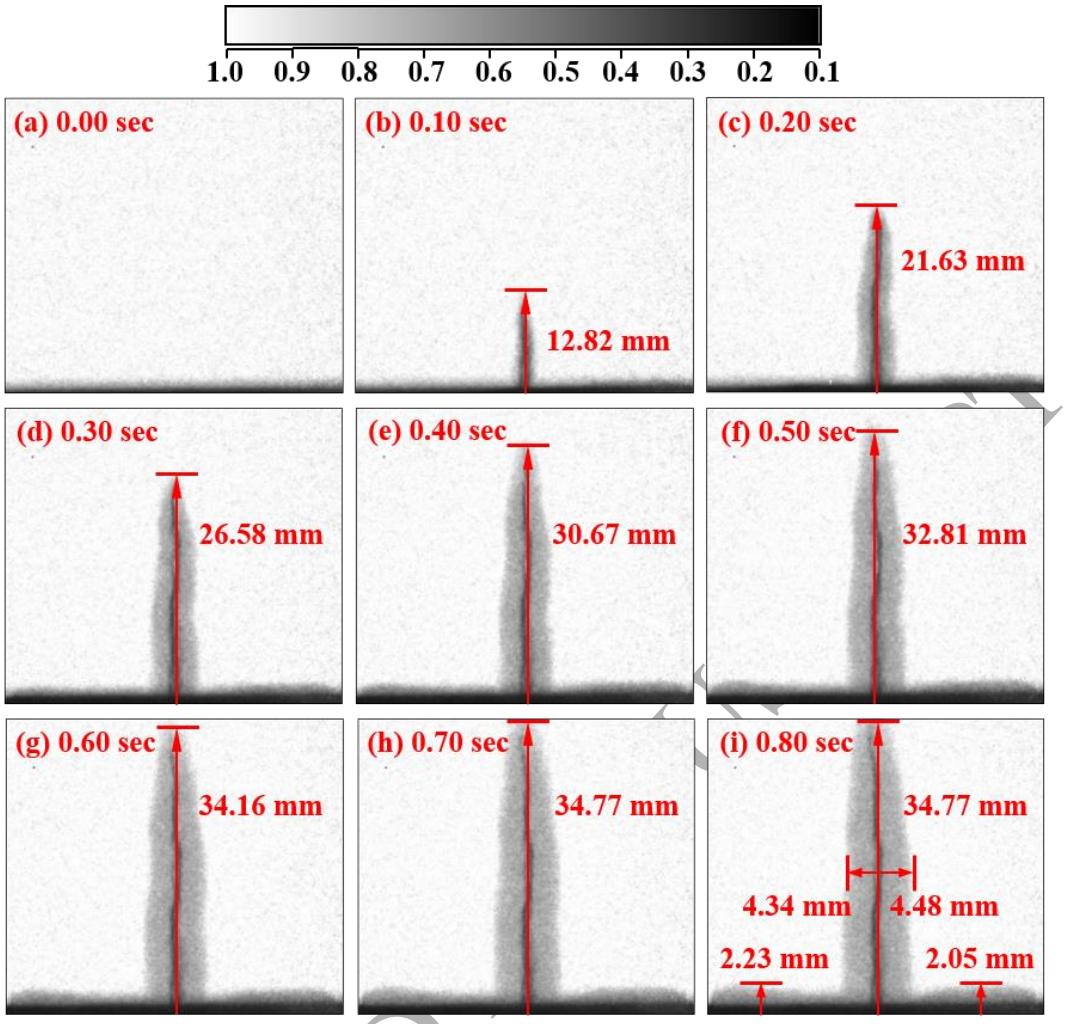

Fig. 7. Selected net water transmission images of water imbibition in the tested specimen W1. Typical images of water imbibition in specimen W1 at continuous time series. These images have been normalized with respect to the initial dry image, so that only water (dark area) is visible.

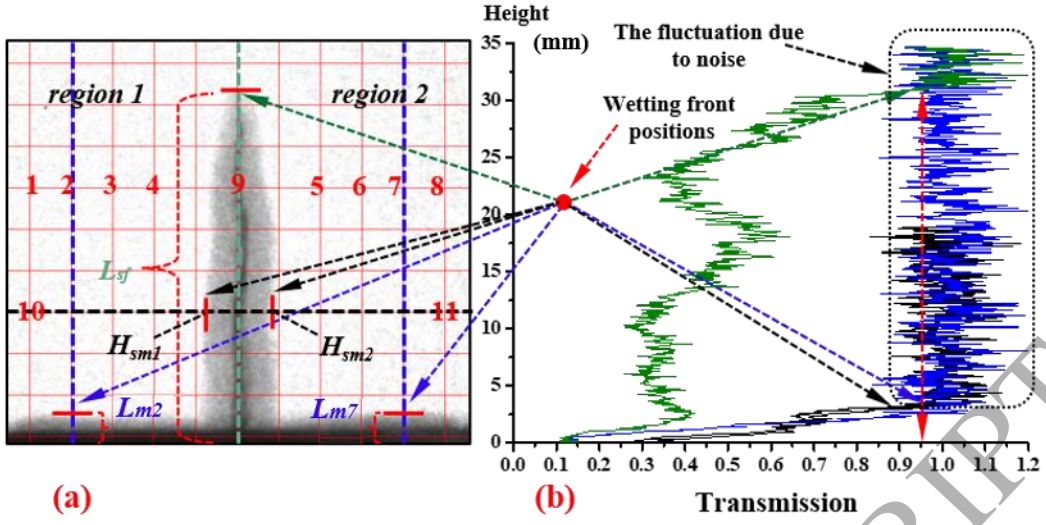

Fig. 8. Schematic of the method for identifying the wetting front in the specimen W1. (a) The positions of vertical net-water transmission profiles (1-9) in specimenW1 and typical transmission image of net water imbibition at 0.40 s. (b) The distribution of the transmission along 2 (blue), 7 (blue), 9 (green), 10 (black) and 11 (black) monitoring lines at 0.40 s. The distances traveled by wetting front in matrix and fracture was indicated as L_{sm1} and L_{sm2} (in vertical direction), H_{sm1} and H_{sm2} (in horizontal direction) and L_{sf}, respectively.

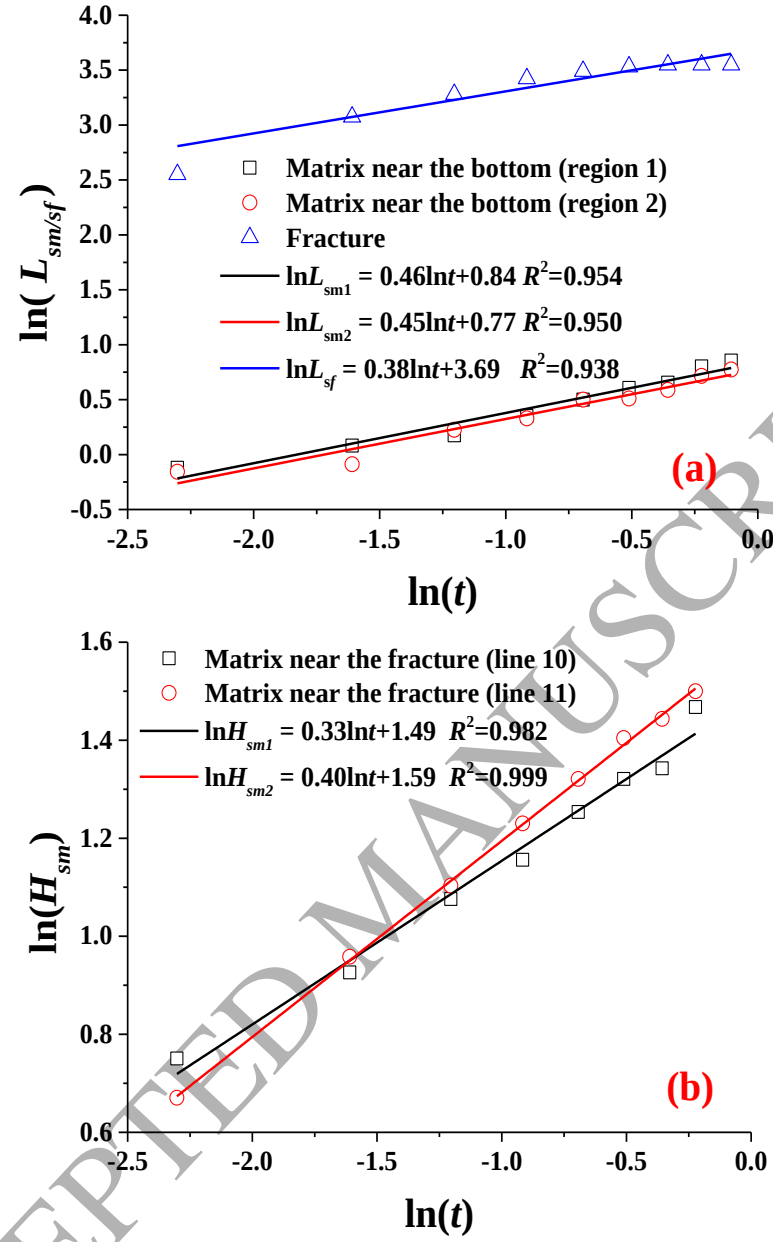

Fig. 9. The log–log plot of the wetting front position versus time in the matrix near the bottom and the fracture zone (a), and the matrix near the fracture (b) of specimen W1.

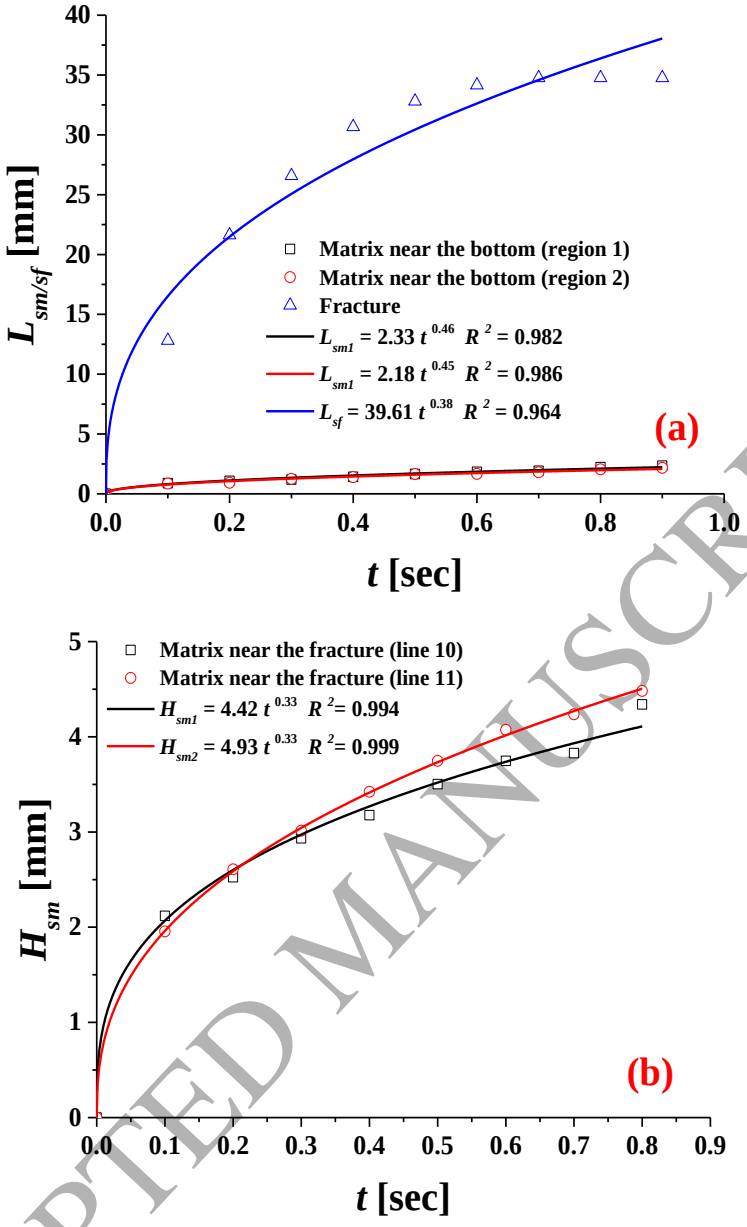

Fig. 10. Wetting front position versus the time for the matrix near the bottom and fracture (a), the matrix near the fracture (b) in specimen W1 measured using dynamic neutron radiography.

List of Tables

Table 1. Mineral compositions of the sandstone specimen W1.

Specimen	Mineral Species and Content (%)		Clay Minerals (%)	Content of Clay Minerals (%)			
	Quartz	Potassium Feldspar		Vermiculite	Illite	Kaolinite	Chlorite
W1	97.4	/	2.6	/	38	62	/

Table 2. The evolution of Porosity (Φ) of specimen based on the CT images with different Thresholds.

Threshold	Φ
1690	0.194221
1691	0.194376
1692	0.194531
1693	0.194688
1694	0.194843
1695	0.194999
1696	0.195155
1697	0.19531
1698	0.195465
1699	0.195621
1700	0.195776

Table 3. The values of distance travelled by wetting front in vertical and horizontal directions, the average volumetric water content and the loss coefficient at different time.

Time (s)	L_{sm1} (mm)	L_{sm2} (mm)	H_{sm1} (mm)	H_{sm2} (mm)	$\bar{\theta}_w$ (mm^3/mm^3)	γ
0.10	0.86	0.86	2.12	1.96	0.16	0.25
0.20	1.08	0.92	2.53	2.61	0.11	0.21
0.30	1.19	1.25	2.93	3.01	0.12	0.25
0.40	1.42	1.39	3.18	3.42	0.12	0.27
0.50	1.65	1.65	3.50	3.74	0.11	0.29
0.60	1.83	1.66	3.75	4.07	0.10	0.29
0.70	1.92	1.80	3.83	4.24	0.10	0.29
0.80	2.23	2.05	4.34	4.48	0.10	0.29
0.90	2.35	2.17	4.48	4.65	0.10	0.32

Table 4. The parameters time exponent α, and the goodness of fit (R^2) for the wetting front motion in Matrix and Fracture of specimen of the wetting process.

Area	α	R^2
Matrix near the bottom (region 1)	0.46	0.954
Matrix near the bottom (region 2)	0.45	0.950
Matrix near the fracture (line 10)	0.33	0.982
Matrix near the fracture (line 11)	0.40	0.999
Fracture zone (line 9)	0.38	0.938

Table 5. The sorptivity of Matrix (C_m) and Fracture zone (C_f) for specimen W1 obtained by Experimental fit, and the goodness of fit (R^2)

Area	α	Sorptivity (mm/s$^{\alpha}$)	R^2
		Experiment fit	
Matrix near the bottom (region 1)	0.46	2.33	0.982
Matrix near the bottom (region 2)	0.45	2.18	0.986
Matrix near the fracture (line 10)	0.33	4.42	0.994
Matrix near the fracture (line 11)	0.40	4.93	0.999
Fracture (line 9)	0.38	39.61	0.964

Table 6. Parameters used to estimate the sorptivity and time exponent of fracture

μ (Ns/m^2)	D	σ (N/m)	θ ($^\circ$)	K (mD)	ϕ (%)	δ (µm)	ξ (µm)	β	$\bar{\theta}_w$ (mm^3/mm^3)	γ	λ_{max} (µm)	λ_f (µm)	τ	τ_f
0.001	1.84	0.0728	0	141	19.5	193.52	390.63	0.01	0.096	0.28	22.76	389	2.06	1.05

Table 7. Comparisons on the experimental and analytical results for the sorptivity of Matrix (C_m) and Fracture zone (C_f).

Area	α	Sorptivity (mm/s$^{\alpha}$)	
		Experiment fit	**Model prediction**
Matrix near the bottom (region 1)	0.46	2.33	2.41
Matrix near the bottom (region 2)	0.45	2.18	2.33
Matrix near the fracture (line 10)	0.33	4.42	1.51
Matrix near the fracture (line 11)	0.40	4.93	1.94
Fracture (line 9)	0.38	39.61	41.20